Simulating the interannual variability of major dust storms on Mars using variable lifting thresholds

Article

Accepted Version

Simulating the interannual variability of major dust storms on Mars using variable lifting thresholds

David P. Mulholland [a,1], Peter L. Read [a] and Stephen R. Lewis [b]

[a] *Atmospheric, Oceanic & Planetary Physics, University of Oxford, Clarendon Laboratory, Parks Road, Oxford OX1 3PU, UK*

[b] *Department of Physical Sciences, The Open University, Walton Hall, Milton Keynes MK7 6AA, UK*

Number of pages: 42

Number of figures: 10

[1] Now at Environmental Systems Science Centre, University of Reading, Harry Pitt Building, 3 Earley Gate, Reading RG6 6AL, UK

Proposed Running Head:

Interannual variability of Martian dust storms

Please send Editorial Correspondence to:

David P. Mulholland

Environmental Systems Science Centre, University of Reading,

Harry Pitt Building, 3 Earley Gate, Reading RG6 6AL, UK

Email: d.p.mulholland@reading.ac.uk

Phone: (+44)7906500365

ABSTRACT

The redistribution of a finite amount of Martian surface dust during global dust storms and in the intervening periods has been modelled in a dust lifting version of the UK Mars General Circulation Model. When using a constant, uniform threshold in the model's wind stress lifting parameterisation and assuming an unlimited supply of surface dust, multiannual simulations displayed some variability in dust lifting activity from year to year, arising from internal variability manifested through surface wind stress, but dust storms were limited in size and formed within a relatively short seasonal window. Lifting thresholds were then allowed to vary at each model gridpoint, dependent on the rates of emission or deposition of dust. This enhanced interannual variability in dust storm magnitude and timing, such that model storms could cover most of the observed ranges in size and initiation date within a single multiannual simulation. Peak storm magnitude in a given year was primarily determined by the availability of surface dust at a number of key sites in the southern hemisphere. The observed global dust storm (GDS) frequency of roughly one in every three years was approximately reproduced, but the model failed to generate these GDSs spontaneously in the southern hemisphere, where they have typically been observed to initiate. After several years of simulation, the surface dust density field showed good qualitative agreement with the observed pattern of Martian surface dust cover. The model produced a net northward cross-equatorial dust mass flux, which necessitated the addition of an artificial threshold decrease rate in order to allow the continued generation of dust storms over the course of a multiannual simulation. At standard model resolution, for the southward mass flux due to cross-equatorial flushing storms to offset the northward flux due to GDSs on a timescale of ~ 3

years would require an increase in the former by a factor of 3–4. Results at higher model resolution and uncertainties in dust vertical profiles mean that this nevertheless appears to be a plausible explanation for the observed GDS frequency.

Keywords: Atmospheres, dynamics; Mars, atmosphere; Mars, surface; Terrestrial planets;

1 Introduction

Atmospheric dust is a crucial component of the Martian climate system, and is a major driver of much of the interannual variability observed in atmospheric temperatures (Liu et al., 2003). Martian global climate models (MGCMs) have, over the past decade, sought to represent this by transporting a radiatively active tracer field, with surface dust sources predicted interactively using parameterisations of dust emission processes (Newman et al., 2002b; Basu et al., 2006; Kahre et al., 2008). These have been broadly divided into two categories: convective lifting, by 'dust devils' (Thomas and Gierasch, 1985), which is thought to provide some or most of the background dust haze that exists throughout the year, and lifting by near-surface wind stress (Bagnold, 1954), believed to be responsible for the generation of dust storms of various sizes (Basu et al., 2006). A strong positive radiative feedback applies to the latter of these mechanisms (Newman et al., 2002a), making it an efficient lifting process, but one which is difficult to simulate accurately.

Modelling studies to date have managed to recreate the distinctly different dust loadings that exist during the clear aphelion season ($L_s \sim 0$–$180°$, where L_s is the solar longitude) and the dusty perihelion season ($L_s \sim 180$–$360°$), by using a threshold-dependent wind stress lifting parameterisation, with the threshold set high enough so as to allow intense dust lifting only during the warmer second half of the year, when all major storms observed have taken place. In most of these studies, the supply of dust at the surface was assumed to be unlimited; therefore, dust emission was dominated by the model gridpoints at which peak surface wind stresses were strongest. This meant that all dust storms generated by the models tended to initiate at the same location, usually

in the vicinity of the Hellas basin (Newman et al., 2002b; Kahre et al., 2008) or in the Acidalia/Chryse regions (Newman et al., 2002b; Basu et al., 2006). The very large interannual variability that exists in Martian dust storm size, timing and location of origin has not been adequately captured by MGCMs, although the models do exhibit a degree of atmospheric variability, which can produce some variation in storm magnitude from year to year if the wind stress lifting parameterisation uses a sufficiently high threshold (Basu et al., 2006). Kahre et al. (2005) modified this approach by initialising each surface gridpoint with a finite surface dust density; however, these simulations were unable to sustain dust storm generation for more than a few model years.

In reality, surface dust densities across the planet are, of course, finite, and probably small enough in certain locations to limit the amount of dust emission that can occur during a large storm. The qualitative spatial distribution of surface dust (particles smaller than $\sim 100\,\mu$m) was derived from Thermal Emission Spectrometer (TES) albedo measurements by Ruff and Christensen (2002), who found the southern hemisphere overall to be more sparsely covered by dust grains than the northern hemisphere. Periodic changes in surface albedo, notably in the wake of major dust storms, were detected by Szwast et al. (2006), indicating the redistribution of significant portions of this surface dust. Furthermore, Strausberg et al. (2005) noted that during the 2001 global dust storm (GDS), dust lifting on the northwestern slopes of Hellas, the site of the initiation of the storm, appeared to cease after ~ 20 sols, while the storm was very much still in progress. Local surface windspeeds remained large at this time (Montabone et al., 2005), raising the possibility that dust sources at Hellas were exhausted of surface dust, preventing further emission from taking place. These changes in surface dust cover may also play an integral role in

driving the strong interannual variability that has been observed in dust storm occurrence and intensity, by introducing into the climate system a long-term memory, something that the Martian atmosphere, with a radiative timescale of order 1 sol, does not possess.

Pankine and Ingersoll (2004) suggested that the removal of dust from a particular area might be equivalent to an increase in the lifting threshold, offering the physical rationale that the local threshold should vary according to the ratio of erodible (dust particles that can be lifted) to nonerodible material present. It may be anticipated that after a burst of emission from a certain site, the dust particles that remain will be those that are sheltered by nonerodible elements, namely rocks and pebbles, and that moving these will require larger wind stresses. Pankine and Ingersoll (2004) found that adding a time-varying threshold prompted hitherto-unseen interannual variability in a simplified global Mars model. Specifically, they used a threshold which increased following a large dust storm, and decreased gradually in the absence of any dust lifting. Suitable tuning of the increase and decrease rates allowed global dust storm frequency to be adjusted to approximately match that currently observed. They suggested that this feedback process, termed 'self-organised criticality', could be an explanation for why Mars appears to be finely tuned to produce GDSs only under certain favourable conditions. However, with the use of a low-order model, with effectively only two surface gridpoints (one in each hemisphere), they were unable to examine storm development or the redistribution process, or ascertain whether or not the approach would work equally well in a fully fledged MGCM. A first attempt at adapting this idea for a GCM was made by Wilson and Kahre (2010), and did produce increased interannual variability in the magnitude of dust storms produced in their model,

though not in the initiation dates of the storms. Also, model GDSs were frequently too large, and occurred in groups every twenty or so years, rather than with a frequency of one every three years, as was estimated by Zurek and Martin (1993) and as has continued to hold true over MY23–28.

The goal of this paper is to include a surface feedback in the wind stress lifting parameterisation of a state-of-the-art MGCM, to attempt to simulate the effect of dust depletion and redistribution on the initiation of large dust storms. The implementation of the feedback, in the form of a variable lifting threshold at each gridpoint, is described, and the improved interannual variability produced by the model as a result is shown. Storm development and surface dust redistribution are analysed, and particular attention is paid to the exchange of dust between the two hemisphere, since this presumably plays an important role in the formation of dust storms over multiannual timescales.

2 Model description

The simulations described in this work were performed using the UK version of the Martian Global Climate Model (UKMGCM) developed through a collaboration between groups in France and the UK (Forget et al., 1999). The UK model uses a spectral solver for the primitive equations (Hoskins and Simmons, 1975), and employs a semi-Lagrangian advection scheme to transport atmospheric dust (water vapour, water ice and other tracers can also be included, if desired). The majority of the simulations were run using the T31 spectral truncation, corresponding to a $3.75^\circ \times 3.75^\circ$ horizontal resolution for the dynamical grid, with physical parameterisations evaluated on a $5^\circ \times 5^\circ$ grid; one additional run used the higher T63 resolution (1.875° for the dynam-

ics and 2.5° for the physics). The model version used was very similar in most of its physical schemes to the one described in Newman et al. (2002a). Dust devil lifting was again modelled by the threshold-independent, convective heat engine parameterisation of (Rennó et al., 1998). However, modifications have been made to the wind stress dust lifting parameterisation, and are detailed below.

A size bin technique was used to lift and transport a size distribution of dust particles. A total of six bins were used, containing six particle radii from 0.1 to 10 μm in the transport simulation of Section 3, and two sets of three radii (0.251, 1.58 and 10 μm) in the subsequent simulations in Section 4. All runs used a radiatively active dust field, with a size-dependent extinction coefficient. The dust lifted from the surface was set to follow a modified-gamma size distribution with an effective radius of $\sim$ 2.5–3.0 μm, which was found to adequately reproduce observed atmospheric effective radii of 1–1.5 μm (Wolff and Clancy, 2003).

2.1 Wind stress lifting with constant threshold stress

As in Newman et al. (2002a), emission of micron-sized dust particles due to wind stress was assumed to occur as a result of impacts from larger ($\sim 100\mu$m) particles in saltation. The upward flux $F(u_*)$ was calculated as

$$F(u_*) = \alpha_N H(u_*),$$

where H is the horizontal (saltation) flux, α_N is the lifting efficiency and u_* is the drag velocity. The drag velocity was calculated from the atmospheric

wind velocity in the lowest model level, $u(z_1)$, as

$$u_* = \frac{\kappa u(z_1)}{\ln\left(\frac{z_1}{z_0}\right)}$$

where κ is von Kármán's constant ($= 0.4$), z_1 is height of the lowest model level ($\sim 5\,\mathrm{m}$ in the UKMGCM) and z_0 is the surface roughness length, assumed to be 1 cm at all gridpoints. A single emission flux was calculated at each gridpoint and combined with the prescribed size distribution mentioned previously. α_N, the ratio between vertical and horizontal fluxes, was kept constant, and its value was tuned to result in realistic dust opacities under storm conditions. The saltation flux was calculated using an approximate fit to recent numerical modelling results of Kok and Renno (2008),

$$H(u_*) = max\left[0, 0.25\frac{\rho}{g}(u_*)^3\left(1 - \left(\frac{u_*^t}{u_*}\right)^2\right)\left(7.0 + 50.0\left(\frac{u_*^t}{u_*}\right)^2\right)\right],$$

where u_*^t is the threshold drag velocity, below which no saltation or dust emission occurs. Compared to the more commonly used formulation of White (1979), this expression provides slightly more 'explosive' dust lifting, by predicting a larger flux for drag velocities just above threshold and a lower flux for larger values of u_* ($\gtrsim 2.5u_*^t$). However, in initial work, similar model performance was obtained using the White (1979) function, indicating that the choice of saltation flux was not crucial to the output of the dust lifting scheme.

Of vital importance to dust lifting predictions is the threshold drag velocity for lifting, u_*^t, used. This was calculated using the theoretical expression derived by Shao and Lu (2000), given by

$$u_*^t = \sqrt{A_N\left(\sigma_p g D_p + \frac{\gamma}{\rho D_p}\right)},$$

where ρ is the atmospheric density, ρ_d is the dust particle density (set to

$2500\,\mathrm{kg\,m^{-3}}$), D_p is the dust particle diameter, $g = 3.72\,\mathrm{m\,s^{-1}}$ is the gravitational acceleration, $\sigma_p = \frac{\rho_d}{\rho}$, and A_N and γ are constants (encompassing particle arrangement, particle Reynolds number at threshold drag velocity and the interparticle electrostatic force) whose values were determined empirically by fitting to wind tunnel data ($A_N \approx 0.0123$ and $\gamma \approx 3{\times}10^{-4}\,\mathrm{kg\,s^{-2}}$; neither value is Earth-specific). This formula can be differentiated with respect to particle diameter to find the minimum threshold velocity, for the most easily mobilisable sand particles,

$$(u_*^t)_{min} = \sqrt{2A_N}\left(\frac{\gamma\rho_d g}{\rho^2}\right)^{\frac{1}{4}}, \tag{1}$$

which applies for particles of diameter $\sim 180\,\mu$m. Saltation was assumed to occur once the drag velocity exceeded (1). The dependence of the threshold velocity on near-surface atmospheric density ($\sim \rho^{-1/2}$) means that this is referred to as a constant threshold stress approach, since surface stress ζ is defined as $\zeta = \rho {u_*}^2$. This is the method that was used by Newman et al. (2005), and in other more recent studies. The threshold calculation did not include any modification due to a non-negligible surface roughness length (maps of which have recently become available). Preliminary work has indicated that this modification produces substantially higher threshold velocities in certain regions, and further study will be necessary to understand how best to accommodate this in a GCM.

Thresholds calculated using equation (1) proved to be too high for lifting by model winds to occur, except in very rare cases. This was not unexpected, as dust emission, since it is a threshold-dependent process, is expected to be dominated by small-scale, infrequent gusts of high windspeed, which are not captured within a typical GCM physical timestep (the time between successive

computations of the dust lifting flux) of ~ 30 minutes and gridbox width of $\sim 100\,\mathrm{km}$. Another important factor in explaining the lack of dust emission under model mean wind stresses is the fact that the impact threshold, u_*^{it}, the drag velocity required to maintain saltation once it has begun, may be substantially lower than the fluid threshold, $u_*^{ft} \equiv u_*^t$, the velocity needed to initiate saltation: Kok (2010) estimated, using a numerical model, that the ratio u_*^{it}/u_*^{ft} could be as low as 0.1. This means that dust lifting fluxes calculated using the larger u_*^{ft} will likely be underestimated, possibly severely so. Both of these effects should be carefully parameterised in future, but for the present case they were combined into a single scaling factor that was applied to the calculated threshold value. The size of this factor was chosen using a tuning process, in which it was required that the development of any dust storms during northern spring and summer be prevented, while allowing emission from a range of gridpoints later in the year. The appropriate factor at T31 resolution was found to be ~ 0.7, which is arguably close enough to unity to provide some confidence in the model mean drag velocities as being representative of the larger gusts within the gridbox that are actually responsible for dust lifting. The threshold wind stress was therefore given by $\zeta^t = \rho(0.7u_*^t)^2 \approx 0.020\,\mathrm{Pa}$. This is close to the value of $0.0225\,\mathrm{Pa}$ used by Kahre et al. (2006), but significantly lower than Basu et al.'s (2006) value of $0.055\,\mathrm{Pa}$, which was chosen to maximise interannual variability in their model and which apparently limited dust lifting (other than during dust storms, when the positive radiative feedback became active) to a very select number of gridpoints.

At each timestep, dust emission fluxes were calculated after near-surface winds had been mixed in the vertical by the model's turbulent diffusion scheme. Dust

was inserted into the lowest model layer, and mixed through the planetary boundary layer by the same scheme. Sedimentation velocities were computed assuming spherical dust particles.

2.2 The variable threshold scheme

The lifting scheme was then modified to allow the dust lifting threshold to vary during the course of a simulation. The threshold stress, ζ^t, was programmed to vary in response to the change in surface dust density at a particular gridpoint, at a rate ${\zeta^t}_{inc}$ (with units of Pa $(\mathrm{kg\,m^{-2}})^{-1}$) linearly proportional to the amount of dust removed or deposited in a physical timestep; that is, the threshold increases as dust is removed from the gridpoint, and decreases whenever dust is deposited onto the gridpoint (the 'inc' suffix is used because, as will be seen later, the dominant effect imparted by this term in key dust source regions in the southern hemisphere is a threshold increase). The true behaviour of stress threshold with changing surface dust density is unknown, so the value of ${\zeta^t}_{inc}$ was chosen simply so that thresholds were raised enough in the course of a large storm to cut off further lifting from at least some gridpoints; similarly, the linear rate of increase was used purely for simplicity. The lifting efficiency α_N and ${\zeta^t}_{inc}$ could to some extent be varied in tandem, as more efficient lifting required faster-growing thresholds to prevent runaway lifting. Various combinations of these two parameters were tested. To prevent lifting from becoming possible outside of the storm season, through year-on-year threshold reduction in dust sink regions, a minimum threshold stress was specified, equal to the original threshold value of 0.020 Pa. Thus, the new parameterisation acted only to increase surface lifting thresholds from the value previously

used. Following the Pankine & Ingersoll argument, this minimum represents a saturation of dust cover in the unsheltered areas of a gridbox, such that adding more dust does not decrease the effective lifting threshold any further.

When the scheme as described so far was applied in a multi-year simulation (with thresholds at each gridpoint initialised at the minimum value of 0.020 Pa), the results were very similar to those of Kahre et al. (2005) (see their Fig. 3), which used a 'straight' finite surface dust method (i.e. without threshold changes). That is, for several model years, major dust storms were produced in a manner largely similar to that seen in previous infinite surface dust work, but dust storms then ceased to occur, and the model became 'locked' into a state that did not feature a significant amount of wind stress lifting in the southern hemisphere. This shut-down of lifting was a result of the threshold increases produced in parts of the southern hemisphere following the removal of surface dust during the storms that occurred in the initial years of the simulation, as dust deposition in these regions evidently did not occur at a sufficient rate to counteract this loss. The time taken to reach this shut-down point decreased as ${\zeta^t}_{inc}$ was increased, since this parameter controls the extent to which thresholds are affected by the removal of a given dust amount (a similar result was shown by Kahre et al. (2005), whereby the decline in global dust opacity could be delayed for a number of years by initialising gridpoints with a deep dust reservoir).

This net movement of dust away from key source regions is a symptom of a more general interhemispheric transport bias, in which dust is transferred from southern to northern hemisphere, that exists in the model, as discussed later (section 5.2). To correct for this bias, so as to allow to continuation of dust storms over multiple model years, another parameter, ${\zeta^t}_{dec}$ (units of

$\mathrm{Pa\,s^{-1}}$), was added, applying a constant rate of decrease to surface thresholds at every gridpoint, in addition to any decreases that occur 'naturally' in the model through deposition of atmospheric dust. This may be interpreted as the continual addition of extra dust to each gridpoint that is above the minimum threshold, so is clearly a crude way in which to counteract the interhemispheric bias. In fact, there is reason to believe that such a term could be justified even in a model without this transport bias, by virtue of redistribution of surface *within a gridbox*. This is discussed in section 5.3. The value for this parameter was set by requiring that some dust lifting remain possible each year and that global dust storms occur approximately every three years. As would be expected, increasing the rate of resupply increases the frequency of large dust storms in the model — approximately,

$$\frac{\zeta^t{}_{inc}}{\zeta^t{}_{dec}} = \frac{\text{gap between successive GDSs}}{\text{surface dust density reduction at initiation sites during a GDS}}.$$

Thus, through these parameters the model could be tuned to try to reproduce the long-term dust storm behaviour that is observed in reality.

Szwast et al. (2006) determined, from MGS surface albedo measurements, that dust devil lifting probably plays little or no role in the redistribution of surface dust. The model's parameterisation of dust devil lifting, however, does produce a net annual dust movement. Furthermore, among the regions that are depleted through the action of dust devils are those that are important in storm generation, such as the latitude band at 30°S. For this reason, the two lifting methods were separated by using two distinct transported dust fields, each made up of three size bins, allowing dust lifted by convective processes to provide the background opacity while ignoring its effect on the surface dust distribution. In part this was motivated by a suspicion that dust devil lifting

in the model could be overestimated, in order to make up for unresolved wind stress lifting events, particularly at L_s = 0–180°. Ideally, dust devil lifting should have been subjected to the effects of changing surface dust densities as well, since dust availability will clearly affect the efficiencies of both lifting mechanisms, but including dust devil lifting in the variable threshold scheme would have required adding a further unconstrained parameter (to convert changes in dust density into some reduction in the dust devil flux, since the scheme is not threshold-dependent), which was undesirable with respect to the simplicity and illustrative ability of the scheme. Also, the background dust haze provided in the model by this mechanism does not need to vary interannually in order to match observations, and it is unknown how much convective lifting varies between years in reality. To be clear, then, surface lifting thresholds in this scheme affected only wind stress lifting, and were themselves affected only by lifting and deposition of dust due to the wind stress mechanism.

3 Results using constant thresholds

The UKMGCM, when run with a prescribed (non-transported) dust distribution that replicates observations from MY24 (Lewis et al., 2007), simulates large wind stresses in several areas known to be important dust sources (Fig. 1), most notably in the region of winter baroclinic activity around 60°N, peaking at Acidalia ($\sim$ 60°W) and at Utopia Planitia ($\sim$ 90°E), and extending south to Chryse and Isidis Planitia, respectively. Peak stresses were also felt in the southwest corners of the Hellas (60°E, 45°S) and Argyre (40°W, 50°S) basins, and at 30°S, the location of the southern summer subtropical jet. These

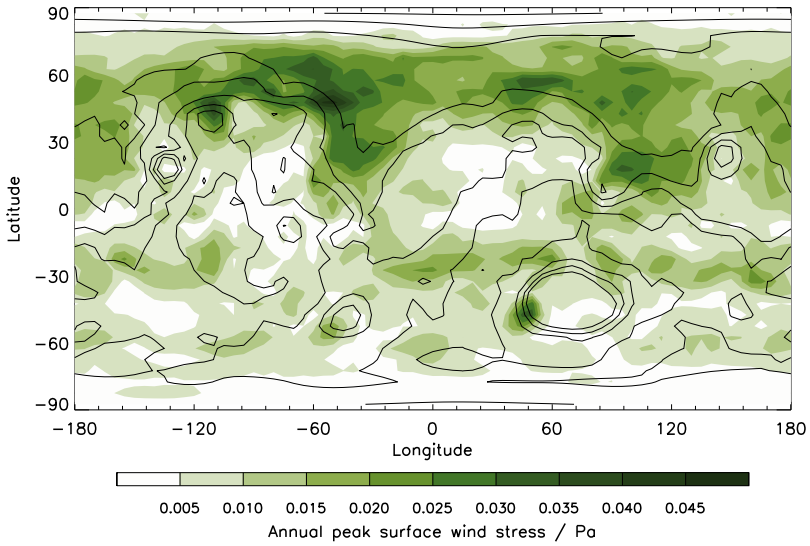

Fig. 1. The maximum surface stress at each gridpoint (in Pa) during a year of simulation without radiatively active dust transport that instead used dust opacities replicating MY24. The Martian topography is overlaid in contours. Only CO_2-ice-free periods were considered when calculating the annual maximum at each point, to make the results more relevant for dust lifting, which is not permitted where CO_2 ice is present.

wind regimes tend to determine the locations of strongest dust emission if the model is run with dust transport assuming an infinite supply of surface dust.

In such a multi-year dust lifting simulation performed using a fixed, homogeneous surface threshold stress, dust storms formed predominantly during the pre-solstice period around $L_s = 210°$–$250°$, beginning with a flushing storm originating at Utopia/Isidis or (less commonly) at Acidalia/Chryse, in the northern midlatitudes. Such events have been regularly observed (e.g. Wang et al. (2005)), and result from frontal cap-edge dust lifting at the boundary of the north polar ice cap and subsequent southward advection along one of three storm tracks, guided by topography to the west (Hollingsworth et al., 1996).

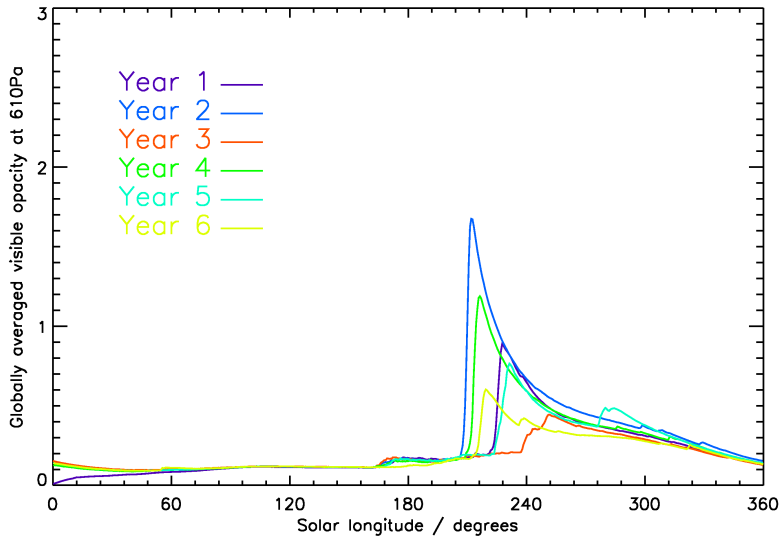

Fig. 2. Globally averaged 610 Pa visible dust opacity from six successive model years, using $\alpha_N = 1.4 \times 10^{-4}\,\mathrm{m}^{-1}$ and $\alpha_D = 9.1 \times 10^{-9}\,\mathrm{kg\,J}^{-1}$.

However, in the model, some of these flushing storms, after crossing the equator, initiated an intense burst of lifting to the north of Hellas (or, in the case of storms travelling south from Chryse, near Argyre), which led to the development of a larger, perhaps planet-encircling, dust storm. This kind of storm initiation has been observed on a slightly smaller scale (e.g. Liu et al. (2003)), and may be the dominant mechanism for the development of regional dust storms; however, observations strongly suggest that global/planet-encircling storms usually begin in the southern hemisphere.

The model produced a limited amount of interannual variability in the timing and peak magnitude of these storms, as shown in the plot of global dust opacity in Fig. 2. However, other than the small second storm in year 5, no significant dust storms formed later than $L_s = 240°$, whereas in reality a large number of such events have been observed to initiate after this date. Another weakness

of this simulation was that there were no instances of a sustained dust loading as large as that of a GDS such as the 2001 storm, which at its peak featured a global visible opacity of greater than 2 (Montabone et al., 2005). This was essentially due to the fact that α_N could not be increased above the value used here without causing runaway dust storm growth. Without any surface dust limit, even very slight increases in α_N were liable to allow dust lifting intensity to increase dramatically through the radiative feedback mechanism, potentially causing the model to crash under very high dust opacities. This high sensitivity to the lifting efficiency has been noted by other workers (e.g. Basu et al. (2006)) and appears to be an inevitable problem when neglecting to include some limit on surface dust availability.

4 Results using variable thresholds

4.1 Interannual variability

The variable threshold scheme was then employed in a multidecadal model integration, using a value for ${\zeta^t}_{inc}$ large enough that the increase in lifting thresholds at a GDS source region is sufficient to shut off further dust lifting at some of these gridpoints during the course of the storm, a value for ${\zeta^t}_{dec}$ chosen to provide the desired GDS frequency of around one every three model years, and using a higher efficiency α_N than before to counteract the larger thresholds (recall that thresholds were allowed only to increase relative to their original value). The stability of the model was greatly improved by the negative feedback on lifting provided by ${\zeta^t}_{inc}$; however, runaway dust lifting, causing a model crash, was still an occasional occurrence, due to very rapid regional

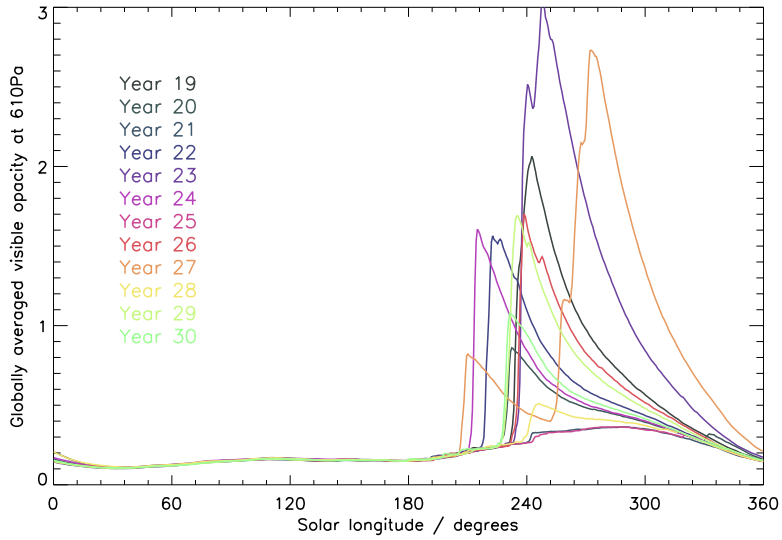

Fig. 3. Globally averaged visible optical depth over several model years (using $\alpha_N = 4 \times 10^{-4}\,\mathrm{m}^{-1}$, $\zeta^t{}_{inc} = 0.5\,\mathrm{Pa}\,(\mathrm{kg\,m}^{-2})^{-1}$, $\zeta^t{}_{dec} = 1 \times 10^{-10}\,\mathrm{Pa\,s}^{-1}$), showing the variation in timing of storm initiation. Year numbering began when the model was properly spun-up with respect to the surface threshold stress field; only the last twelve years of the run are shown.

opacity increases during the initiation of major storms in certain cases. In order to successfully carry out the multidecadal simulation, a condition was added to the wind stress lifting scheme to shut off dust lifting at any gridpoint where the column visible opacity exceeded 10, as a last resort to prevent a crash in these select instances. This condition therefore slightly limited the rate of expansion of GDSs in a few years of this long run, but is not expected to have affected the peak global opacity attained or the decay phase of the storms, since such large local opacities are only possible during an explosive lifting phase at the beginning of a storm.

Fig. 3 shows a 12-year sample of the longer, multidecadal simulation, which was begun after a number of spin-up years during which the threshold field

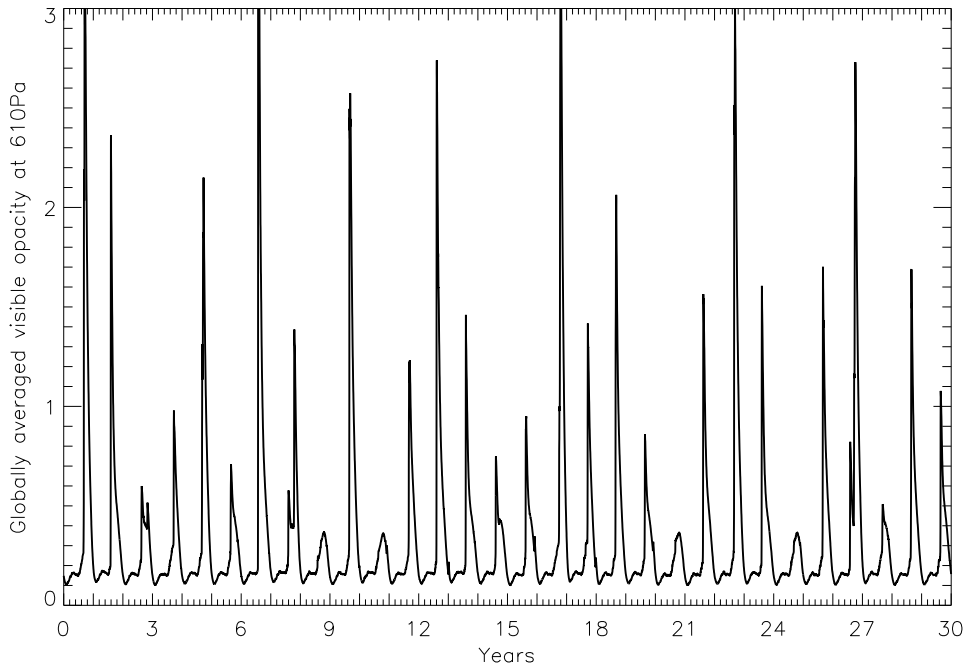

Fig. 4. Globally averaged visible optical depth over a period of thirty model years.

reached a quasi-equilibrated state (see Figs. 5 & 6). Interannual variability in dust storm magnitude and initiation date increased dramatically, in comparison to the unlimited surface dust simulation of Fig. 2. Over the full duration of the run, large dust storms (those producing a globally averaged visible opacity of greater than ~ 1) began at dates in the range $L_s = 205°$–$280°$. This represents a significant portion of the observed window for global storm occurrence: the only GDS known to have initiated later than $L_s = 280°$ was that of 1924 (Phillips, 1924). Even the largest model storms decayed sufficiently rapidly — through a combination of lifting being made more difficult by increasing threshold stresses and a reduction in surface winds due to increased atmospheric static stability under high dust loadings — so as to return global opacity levels to their standard 'background' state of ~ 0.2 by $L_s = 0°$, in agreement with observations.

Fig. 4 shows the chronological progression of globally averaged opacity over thirty model years. The peak opacity attained in a given year clearly depends strongly on the size of the storm that was produced in the previous year, as the largest storms tended not to occur in successive years. A rough periodicity of 4–7 years can be discerned from the plot, but the time series in opacity nonetheless appears somewhat chaotic. If global dust storms are defined as those for which global opacity reaches ~ 2, then the '1 in 3' observed frequency of occurrence was roughly replicated by the model in this case. However, also present were a significant number of model years in which opacity exceeded 1 (19 of the 30 years shown), resulting from dust loadings which were too large to be said to be typical of the regional storms that usually occur in non-GDS years (see Fig. 4, Montabone et al. (2005)). Observations seem to indicate a separation in size between global and regional dust storm peak opacities (though not decisively so, as yet), which the model did not simulate.

We note that the radiative properties used in this experiment describe dust that is now known to be 'too dark' in comparison to the most recent observations (Wolff et al., 2006), implying that the atmospheric heating rate for a given dust loading was too large. This can be anticipated to have made both the positive radiative feedback mechanism, which applies in the initial stages of dust lifting, and the isothermal-atmosphere shutdown mechanism, which aids the decay of GDSs, too strong. It would therefore be desirable in future to repeat the experiment using the most up-to-date dust radiative properties, to see if the peak storm opacities produced by the model are much altered, or if the speed of storm development is affected. For this reason, particular years in Fig. 4 should not be identified with any particular real-life GDS by virtue of having a similar globally averaged opacity. The classification of model years

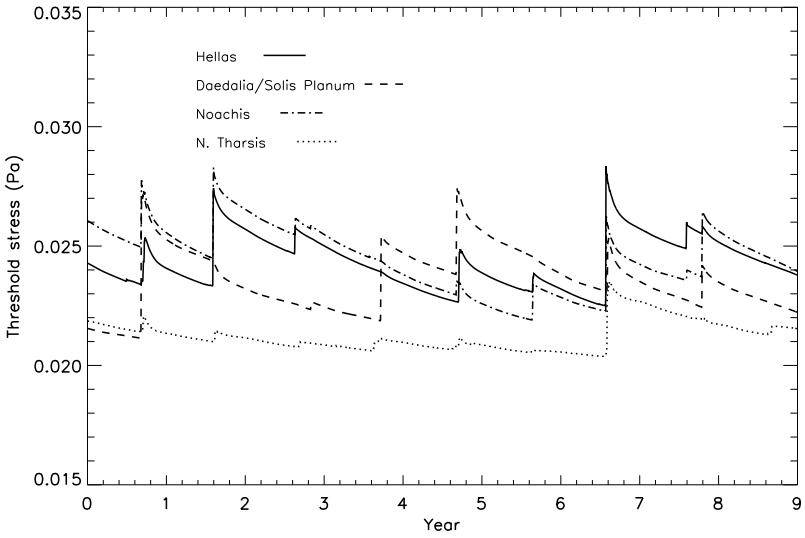

Fig. 5. Behaviour of threshold stresses averaged at key lifting regions over a portion of the multidecadal run (the first nine years shown in Fig. 4).

as being with or without a GDS is unaffected, however, as GDSs can also be identified by the widespread dust lifting that is produced in their formation and by the spread of elevated dust loadings across a wide range of latitudes, evidence of both of which is given later in this section.

4.2 Surface dust redistribution and threshold changes

The contribution of various locations on the planet to storm generation is highlighted in Fig. 5, which shows the threshold stress variation in response to dust lifting from several key regions. As before, large dust storms generally began when a flushing storm from the northern hemisphere (originating in Acidalia or Utopia) crossed the equator, whereupon lifting was initiated in the southern midlatitudes, usually either near Daedalia Planum or northeast of the Hellas basin. Often lifting was subsequently activated over large parts

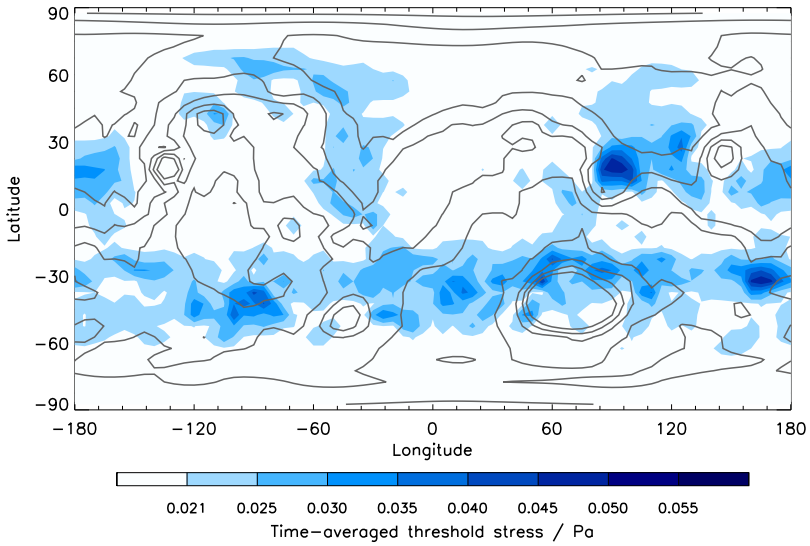

Fig. 6. The climatological threshold stress field, estimated using the model field averaged over 6 years. Thresholds in sink regions are always close to the minimum allowed value of $\sim 0.02\,\mathrm{Pa}$, while source region thresholds are permanently elevated.

of the southern midlatitudes, as seen in the coincident rising of thresholds at the three southern hemisphere sites shown, during certain years. During other years (e.g. in the fourth year plotted), smaller events began at one of the sites (again, usually sparked by a flushing storm, though not always), but failed to become planet-encircling, at least in part due to the thresholds at the other sites being too high to allow the sites to become involved in dust lifting. The value used for ${\zeta^t}_{inc}$ was $0.5\,\mathrm{Pa}\,(\mathrm{kg\,m^{-2}})^{-1}$, which led to rises of up to $0.005\,\mathrm{Pa}$ in the effective (i.e. following the reduction by a factor of $(0.7)^2$) threshold stresses at the SH lifting sites (area-averaged; individual points could increase by $0.015\,\mathrm{Pa}$ during an intense burst of lifting). Threshold stresses fluctuated about a mean value of $\sim 0.025\,\mathrm{Pa}$, as seen in Fig. 5. Thus, variations of no more than $\pm 15\%$ about this mean value were sufficient to affect drastically the resulting dust storm behaviour.

The spatial distribution of time-mean thresholds can be thought of as representing a climatological surface dust field, about which anomalies in dust density occur from year to year and affect the ability of various source regions to supply dust to the atmosphere. This mean state, shown in Fig. 6, featured large threshold stresses, equivalent to low surface dust densities, at regions similar to those that saw high wind stresses in Fig. 1. Significant threshold increases were seen over 15–45°S (the location of the summer subtropical jet), and along the topographic channels at Chryse, Isidis and Amazonis, denoting persistent dust lifting. Conversely, the low thermal inertia (TI) 'continents' at Amazonis/Tharsis, Arabia and Elysium were net accumulators of dust (grid-points that remain at the minimum allowed threshold can be inferred to be sink regions), particularly on their eastern edges. Differences between this spatial pattern and the peak wind stress distribution of Fig. 1, taken from a non-storm, passive dust run, highlight the effect of lifting feedbacks, principally an intensification of the southern subtropical jet during spring/summer dust storms. Conversely, the large wind stresses seen across 40–70°N in Fig. 1 have not translated into widespread dust loss, as most of the dust lifted at these latitudes is advected primarily by the circumpolar flow and is deposited again at a similar latitude. The source regions seen here correlate well with those suggested in the Dust Cover Index (DCI) of Ruff and Christensen (2002) (see their Fig. 14). Though only a qualitative measure of surface dust depth, it indicates that the low-TI continents are very dusty, while most of the southern hemisphere and the Chryse and Utopia flushing channels are relatively depleted of dust. The similarities between the model surface threshold field and the observed DCI over most of the planet suggest that the current surface dust cover can be explained by the action of present-day wind regimes, rather than requiring the invocation of a past climate state to redistribute dust so

as to produce the present DCI. However, possible long-term transport due to dust devil lifting is not considered in this reasoning.

4.3 Analysis of sample model dust storms

As an example of the nature and the causes of the interannual variability produced in the model, dust storms from two successive years, both of which began in the pre-solstice period at $L_s = 230$–$250°$, are shown in Fig. 7. Both cases began with a flushing event in the Chryse region, but the subsequent developments were very different. In the first year shown, a burst of dust lifting occurred at 55°N, 45°W at $L_s = 243°$, coincident with a local increase in transient wave activity, producing a local visible opacity of > 2, and the resulting storm moved southward from Chryse towards Solis Planum. It reached $\sim 60°$S, south of Daedalia Planum, and dissipated after 10 sols. A second lifting event was seen soon after, again at Chryse, but failed to develop into a flushing storm. In the second year, the lifting that led to storm formation occurred earlier ($L_s = 231°$) but in the same location as in the previous year. The peak in opacity was larger in magnitude and spatial extent than before, but flushed southward along a similar path. However, on this occasion the storm grew in strength as it crossed the equator, and upon reaching Solis Planum it sparked intense dust lifting at a number of gridpoints (sol 459). The storm then grew rapidly, spreading westward by activating further lifting sites around Daedalia and Sirenum ($\sim$ 45°S, 150°W), and also moving eastward into northern Noachis. The initial lifting at Solis Planum only lasted for a few sols before dropping out, by which time neighbouring regions had taken over as dust sources. The storm became planet-encircling at around $L_s = 238°$,

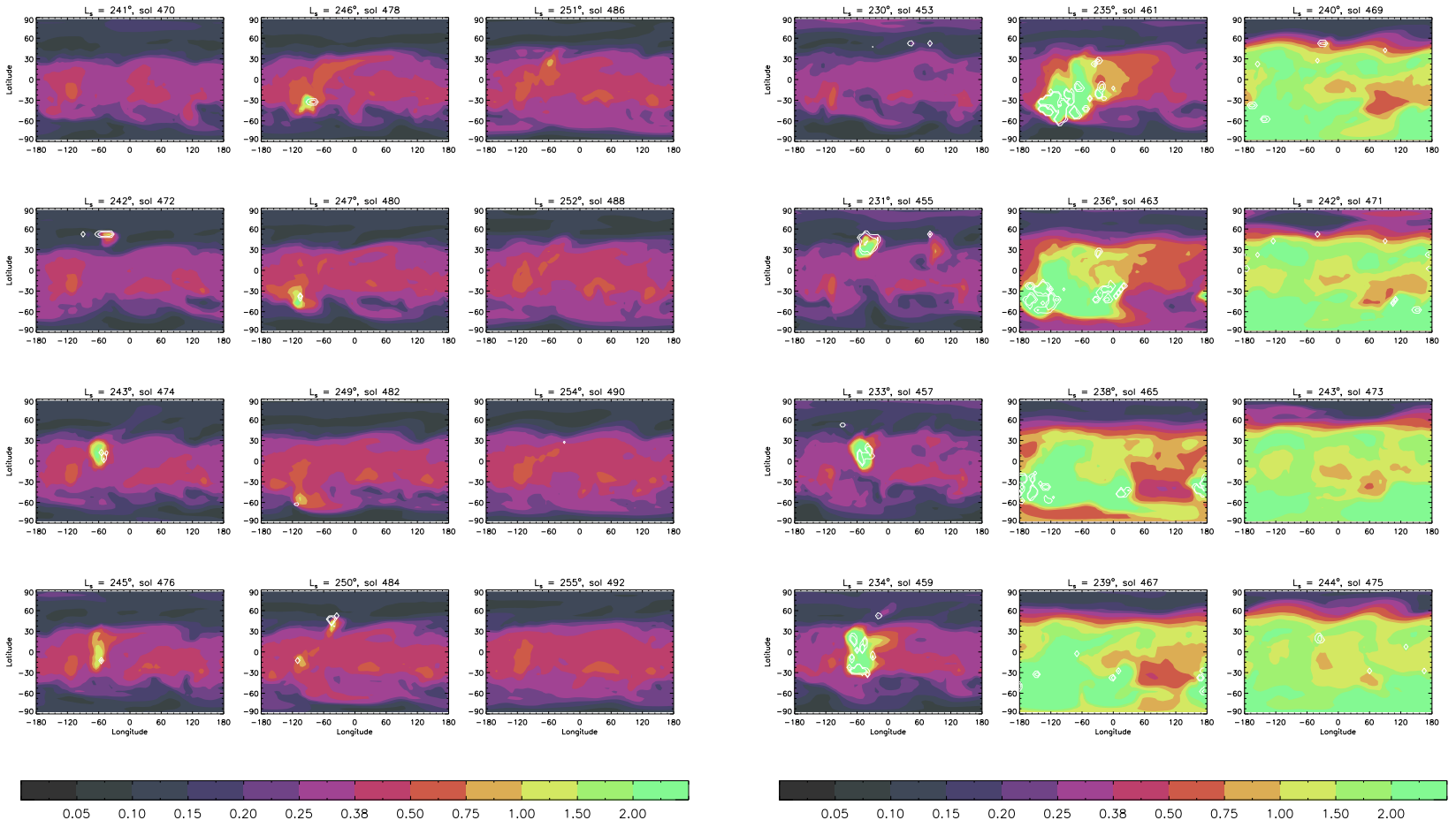

(a) (b)

Fig. 7. Progression in 610 Pa dust opacity from two successive years of the longer simulation. White contours mark where wind stress dust lifting is occurring, with contour levels of $(10^{-8}, 10^{-7})\,\mathrm{kg\,m^{-2}\,s^{-1}}$.

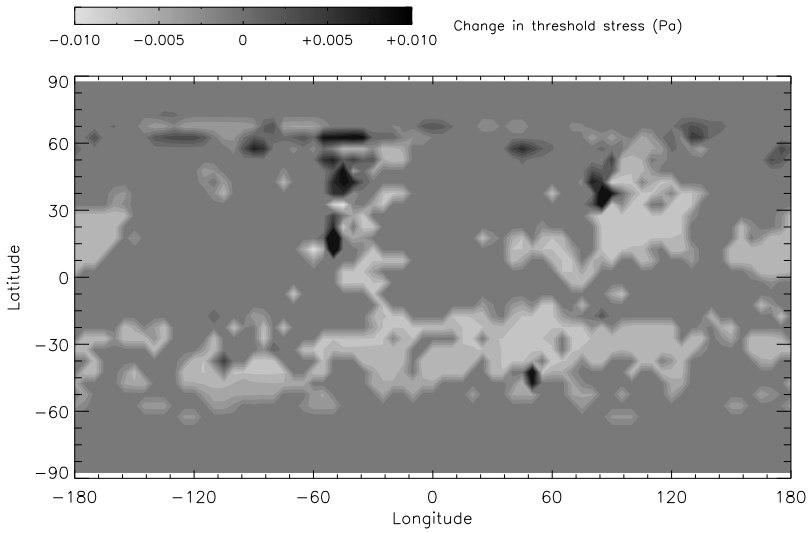

Fig. 8. Difference in threshold stress (Pa) between $L_s = 240°$ in the first year and 230° in the second year, showing the enhanced potential for lifting in the southern hemisphere at the beginning the second storm season, in comparison to the first (regions that see little change in threshold are typically sink regions with thresholds already at the minimum value).

15 sols after initiation, and covered most of the globe at its maximum extent. Global opacity began to decline as early as $L_s = 240°$, when lifting had largely stopped at the Solis/Daedalia sites, but did not return to the 'background' level until $L_s = 330°$.

Mean surface stresses over much of the planet were very similar at the beginning of each of the storms, and transient eddy stresses, which are important for producing bursts of dust lifting, were actually larger in the first year than in the second, particularly at Acidalia. Rather than any differences in wind patterns, the main reason for the expansion of the flushing event into a GDS in the second year only was the lower threshold stresses that existed at $\sim 30°$S by spring, in comparison to the previous year (Fig. 8). While some increases

in threshold were seen at Chryse due to the lifting that occurred during the first year, elsewhere thresholds were reduced, by more than 0.005 Pa, due to the action of the resupply term over the intervening period. This change made a burst of lifting at Daedalia much more likely, and also facilitated the growth of the dust storm, as this initially occurred along the 30–60°S band through the activation of secondary dust lifting sites. The importance of the threshold stress to the development of large dust storms was tested by rerunning the second year after replacing the threshold stress field at the start of the year with the (larger) values from the start of the first year (i.e. negating the action of the resupply term and any dust deposition over the course of the first year). The resulting storm again began near Chryse, but was much more limited than the original second year storm, with a peak globally averaged opacity of less than 1. The magnitude of this storm lay between the magnitudes of the storms in the first and second years above, indicating that dust lifting is controlled by a combination of interannual variability in wind stress and variation in the threshold stress.

Shown in Fig. 9 are transient surface stresses, filtered to include only signals with periods of 1.5–10 sols (to isolate midlatitude baroclinic waves), during the onset and development of the storm shown in Fig. 7(b). Transient stresses increased over large areas of the southern hemisphere (particularly near Daedalia) during the initiation phase of the storm ($L_s = 230$–$238°$), and then began to decrease once the storm had become planet-encircling, as atmospheric static stability increased under the high global dust opacity that developed. Interestingly, rises in transient eddy activity at Daedalia over sols 453–459 preceded the increase in local opacity, and undoubtedly played a role in the intense lifting that did occur when the flushing storm arrived at sol 461,

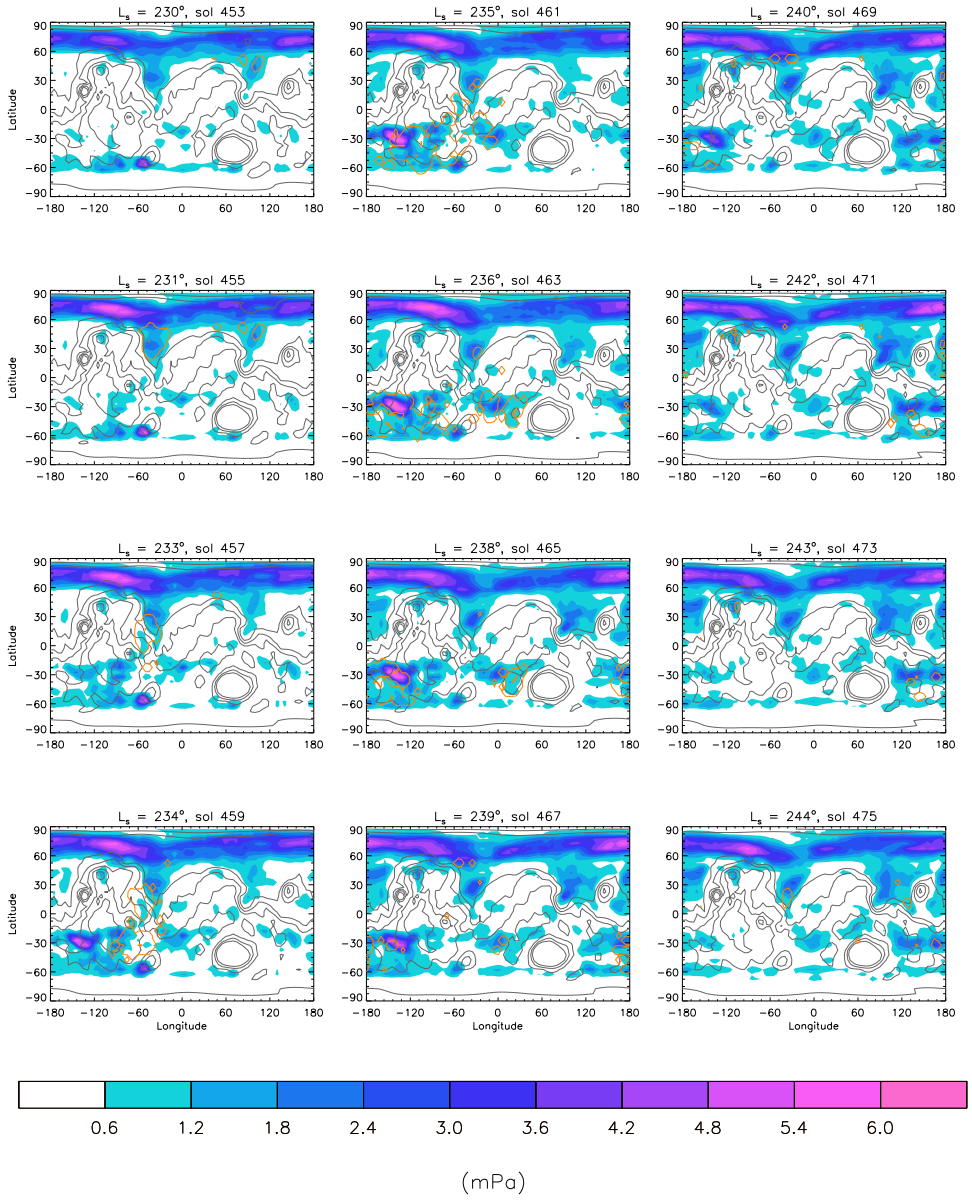

Fig. 9. Time series of transient (period 1.5–10 sols) surface stress (in mPa) during the development of the dust storm in the period shown in Fig. 7(b). The $10^{-8}\,\mathrm{kg\,m^{-2}\,s^{-1}}$ dust lifting rate contour is marked in orange — areas showing lifting in the northern hemisphere can be used as a rough indicator of the leading edge of the flushing dust cloud.

though they were not sufficient to cause any lifting prior to its arrival. This appears to be an example of a 'transient teleconnection' event, somewhat similar to that described by Martínez-Alvarado et al. (2009), but with information transmitted primarily in the meridional rather than the zonal direction. Upon investigation, it was found that a similar advance wave response can be seen in the TES reanalysis dataset (Lewis et al., 2007) during the southern spring flushing storms that occurred in MY24 and MY26. It is possible that this effect operates in a similar manner to teleconnection patterns on Earth, but on a much shorter timescale ($\lesssim 5$ sols), with peaks in diabatic heating localised at the site of the dust cloud playing a role analogous to that of sea-surface temperature anomalies.

4.4 Interhemispheric dust transport

The ease of production of dust storms in the model depends ultimately on the movement of surface dust between the two hemispheres. For a major storm to occur requires sufficiently low thresholds at one or more of the key southern hemisphere initiation sites, but the need for the resupply term ${\zeta^t}_{dec}$ in the simulation described above makes it clear that threshold reduction did not occur sufficiently rapidly, if at all, through dust deposition in these areas. By comparing lifting and deposition rates and atmospheric loadings in each hemisphere, the net cross-equatorial transport rate could be estimated. It was found to depend strongly on both the size and timing of the dust storms that occurred in a given year. Averaged over the last six years shown in Fig. 3, the overall northward cross-equatorial transport rate was $7 \times 10^{10}\,\mathrm{kg\,yr^{-1}}$, though around 60% of this was attributable to dust devil lifting, which was

excluded from the variable threshold scheme. Only dust lifted by wind stress lifting was allowed to affect lifting thresholds — the net transport from this was also northward, at an average rate of $3 \times 10^{10}\,\mathrm{kg\,yr^{-1}}$ but with a high degree of variability between individual years, as seen in Fig. 10. This explains why the resupply term was needed to sustain dust storm activity over a long simulation: dust lifted by wind stress was being 'lost' from the areas from which it could be lifted subsequently, primarily to the low-TI regions and northern high latitudes. The value for ${\zeta^t}_{dec}$ that was necessary to allow GDSs to continue to form with the desired frequency was found to be $\sim 1 \times 10^{-10}\,\mathrm{Pa\,s^{-1}}$, which equates to a global dust resupply rate of $4.75\,\mu\mathrm{m\,yr^{-1}}$. (Due to the minimum threshold imposed, dust falling on a gridpoint whose threshold was already at that minimum value was truly lost from the system, but this loss was estimated globally to be $0.1\,\mu\mathrm{m\,yr^{-1}}$, so it accounted for only a small part of the resupply term.)

Cross-equatorial transport followed, in general, the direction of the upper branch of the principal meridional overturning cell (PMOC), from summer to winter hemisphere. This meant that dust lifted during a major storm was transported out of the southern hemisphere, and efficiently so, since the PMOC is stronger around perihelion (southern spring/summer) than it is at aphelion. There was also, however, significant transport in the opposite direction in the lower branch of the PMOC, which was enhanced when a flushing storm occurred. This allowed years without a major dust storm the possibility of producing a net southward movement of dust lifted by wind stress, though the overall transport (considering both lifting mechanisms) remained in the northward direction, due to the relatively inefficient transport of dust — lifted mainly by dust devils — out of the northern hemisphere over $L_s = 0$–$180°$.

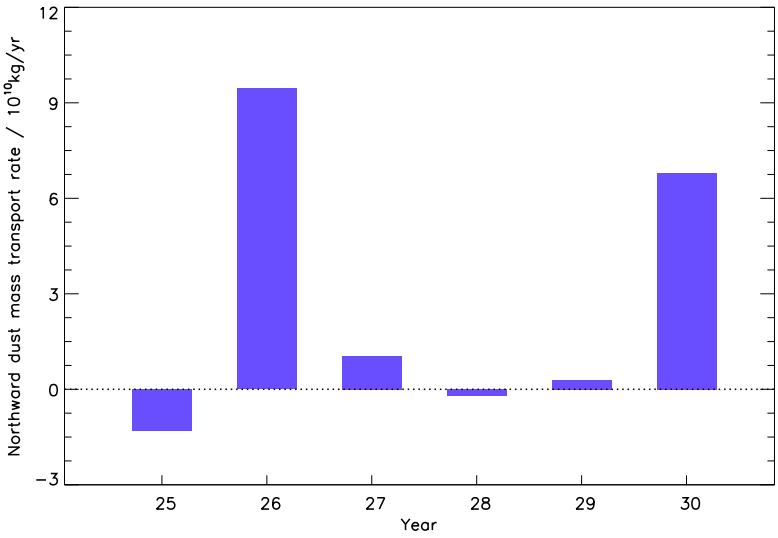

Fig. 10. The net rate of transfer of dust, lifted by wind stress, from the southern hemisphere to the northern hemisphere (in $10^{10}\,\mathrm{kg\,yr^{-1}}$), in each of six model years. The uncertainties associated with the calculations are sufficiently low that the direction of the net transport in each year has been robustly determined.

Again, flux towards the winter hemisphere in the upper part of the PMOC was partially offset by transport in the opposite direction nearer the ground; in fact, this offset was more substantial, due to the weaker vertical mixing of dust at this time of year, in comparison to the dusty season.

Several further model years were run at the higher T63 horizontal resolution, by interpolating the threshold field and dynamical fields from the end of the T31 multidecadal simulation. Some caution is required with the interpretation wind stress lifting patterns in these results as, due to computational constraints, the simulation was not continued for long enough to ensure that the threshold field had adjusted to the wind stress lifting patterns of the higher resolution model. Nonetheless, some significant changes to both types of lifting patterns were apparent. It was seen that wind stress dust lifting rates were

increased, due to a superior resolution of small-scale wind variability compared to the standard T31 case. In particular, lifting at the north polar cap edge was enhanced over $L_s = (0–60, 180–360)^\circ$, meaning that flushing storms were produced with greater regularity. In the first year of the run, which did not feature any major dust storms, the net flux due to wind stress lifting was strongly southward, and was increased by a factor of five over a similar non-GDS year at T31, due mainly to the occurrence of five flushing storms during the dust storm season. In this particular year, the overall dust flux was also in the southward direction, as the net (northward) transport due to dust devil lifting was reduced by $\sim 50\%$ compared to the T31 case. This occurred primarily through a larger southward flux over $L_s = 0–180^\circ$, produced by a combination of a decrease in SH dust lifting relative to the NH and a slightly expanded PMOC. The implication of this sensitivity of cross-equatorial transport to resolution is discussed in the next section.

5 Discussion

5.1 Dust storm characteristics

Several important deficiencies remained in the model's representation of dust storm characteristics. Very rarely did a dust storm develop spontaneously in the southern hemisphere, as has been observed on numerous occasions on Mars (such events were seen occasionally in the model, in Noachis or Daedalia, but these storms never grew particularly large). Instead, the largest storm that formed in a given year usually did so following the arrival in the SH of a flushing storm, with the peak magnitude of the major storm being determined

by the state of the threshold field in that particular year. This meant not only that the model did not distinguish between initiation mechanisms for regional and for global storms, but also that the sizes of these two kinds of storms were not distinctly different. In truth, the number of well-observed Martian years of dust storm activity to date does not allow a clear assessment of whether or not there does exist a separation in peak opacities between regional and global storms. However, there does appear to be evidence that the two types of storms tend to begin in different locations, in the sense that several GDSs are known to have formed in the SH (notably at Hellespontus, Argyre and Noachis), while flushing events, originating in northern midlatitudes, have so far been much more limited in their peak extent. The lack of major dust storms originating in the SH in the model is likely to be a result of under-resolved mesoscale circulations around the topographic features of the region (as suggested also by Basu et al. (2006)), in particular the basins at Hellas and Argyre. The importance of slope winds, and thermal contrast flows near the edge of the south polar cap, in raising dust around Hellas probably explains why no dust storms could be generated as early as the 2001 GDS (which began shortly after $L_s = 180°$). It may be necessary, in future, to parameterise these effects in some way, if the strongest surface wind stresses at key storm initiation sites are to be adequately simulated in an MGCM.

The model often produced either a regional or global storm during $L_s = 210$–$240°$, which is known to be a particularly dusty season (Liu et al., 2003), but modelled global storms after 240° were fairly rare, while several of those observed (MY9, MY12, MY28) have begun at $L_s = 260$–$270°$. The most obvious explanation for this deficiency is that the model had usually produced a large storm earlier in the year, whereupon the decrease in surface winds in the dusty,

isothermal atmosphere made it difficult to produce any more dust storms until the original event had cleared. None of the three years mentioned above are known to have featured a large dust storm beginning as late as $L_s \sim 230°$, as generally occurred in the model; furthermore, it is interesting that the one example of a post-240° GDS in Fig. 3 (in year 27) was preceded by a storm that began unusually early, at $L_s \sim 205°$, and had almost fully decayed by 250°.

It is also notable that no recorded planet-encircling storm has begun during 210–240°. This suggests that the pre-solstice storms shown in Fig. 3 tended to grow too large, and also highlights that their genesis, from flushing events that cross the equator, was unrealistic. The excitation of dust lifting in the SH upon the arrival of a flushing storm was evidently stronger in the model than it ought to be.

Finally, there was a lack of late-summer (post-300°) regional storms in the simulation described above, but further work has suggested that these events are quite sensitive to changes in model physics and/or horizontal resolution. In the present case, their production may have been hindered by NH dust opacities that were slightly too large, following increases earlier in the year during dust storms that had not fully decayed by $L_s \sim 300°$, which would tend to weaken circumpolar baroclinic eddies.

5.2 Interhemispheric transport

The differences in annual transport between the four 'dust storm' years in the 6-year T31 series were surprisingly large: net interhemispheric mass transport

did not simply depend on peak storm magnitude. In this limited sample, the most efficient south-north transport occurred during $L_s \sim 210$–$240°$, and the cross-equatorial flux was higher when the dust storm began in Noachis or Daedalia than when it began at other longitudes. Taking the average of these years (each featured a peak visible opacity of at least 1) as a rough estimate of the northward wind stress transport during a GDS year gives a value of $\sim 4.5 \times 10^{10}\,\mathrm{kg\,yr^{-1}}$, while the two non-storm years provided a flux of only $\sim 0.6 \times 10^{10}\,\mathrm{kg\,yr^{-1}}$ in the opposite direction. It is not known on what timescale the cycle of dust transfer between the hemispheres is closed, but the scheme used here has implicitly assumed that it is around three years, since each initiation site in the SH could not support more than one GDS before requiring replenishment in subsequent years. Therefore, given the typical observed ratio of two non-GDS years to every one GDS year, the southward flux during the former would need to be around half as large as the northward flux in the latter, in order to support continued GDSs in the model without the need for the resupply term. This would require an increase of a factor of 3–4 in flushing storm transport.

However, cap-edge lifting and flushing storm frequency are almost certainly underestimated at T31 resolution, and a much larger southward wind stress flux ($\sim 7 \times 10^{10}\,\mathrm{kg\,yr^{-1}}$) was recorded in a non-GDS year at T63 resolution. The occurrence of five flushing storms in a single year is probably unrealistic (Wang et al., 2005), so a more reasonable estimate of the north-south mass flux due to flushing storms at T63 might be $(3$–$4) \times 10^{10}\,\mathrm{kg\,yr^{-1}}$. This would still be enough to offset the northward GDS flux within the required timescale, even allowing for additional northward transport due to regional storms in the southern hemisphere, as occurred in year 28 of the T31 sequence shown above.

It is apparent that the net dust flux across the equator depends very much on the vertical distribution of dust mass in the tropics, and in this regard dust transport was most likely biased towards the northern hemisphere, since the model did not reproduce the dust mass mixing ratio profiles seen around aphelion by Mars Climate Sounder (Heavens et al., 2011). These profiles featured elevated dust maxima at 20–30 km above the surface, but model profiles showed dust to be fairly well-mixed up to $\sim$ 15 km, with mixing ratios decreasing with increasing height above this level. Therefore, too much model dust was concentrated close to the surface (below $\sim$ 5 km), from where it was advected from winter to summer hemisphere by the lower branch of the PMOC. This must have been part of the reason for the strong net northward flux that was seen at T31 resolution for dust lifted by dust devils. Differences in vertical mixing may also partly explain why the dust devil flux reported by Haberle et al. (2006), using a similar lifting parameterisation in the NASA-Ames model, was in the opposite direction (strongly southward) to the one calculated in this work. The result is puzzling, however, and indicates that the global-scale effects of dust devil lifting and transport are not well constrained at present, justifying the decision to exclude its influence from the variable threshold scheme. The significant difference in dust devil flux between the T31 and T63 resolutions lends further support to this decision. In reality, considering the abundances of dust seen in the MCS profiles at 20–30 km in the northern summer tropics, a significant amount of southward dust transport may occur over $L_s = 0$–$180°$, further assisting the return to the southern hemisphere of dust lost during a GDS.

It is necessary to justify the use of the artificial 'resupply' term by interpreting its possible physical meaning. As stated previously, the term was introduced for pragmatic reasons, to prevent the model from becoming locked in an unrealistic, low-dust state during a multidecadal simulation. The reason for its need was identified in the previous section as the long-term model mass transport bias towards the northern hemisphere, which must inevitably lead to the cessation of dust storms in the southern hemisphere if a finite surface dust supply is used. In choosing the value of ${\zeta^t}_{dec}$ to allow GDSs to occur approximately every three years, we have assumed that the interhemispheric transport is close to zero on this timescale — this may not be true, but the existence of a large net cross-equatorial flux would seem to be difficult to explain, given that most GDSs have been observed to originate in a region of the SH where dust is known to be in relatively short supply.

The proper way to correct this model transport bias, if it is indeed a bias compared to reality, is through model improvement, and we have highlighted vertical profiles as a potential area of importance. However, the need for a parameterised reduction in threshold (equivalent to an increase in available dust) can extend beyond the crude correction of transport bias. The introduction of the scheme by Pankine and Ingersoll (2004) suggested that a decrease in threshold over time could be caused by a redistribution of the surface dust layer on a microscale level, as dust is shifted out from sheltered locations (near nonerodible elements) into areas from which it can more easily be mobilised by the winds. In a GCM, such a process would occur via sub-gridscale winds, and must therefore be parameterised. An alternative interpretation of

the threshold decrease term comes from recent suggestions that — contrary to the canonical approach taken by modellers to date — saltation does not occur particularly often on Mars, and that dust lifting instead occurs through direct detachment of low-density, sand-sized dust aggregates (Sullivan et al., 2008). The availability of dust for lifting from a particular gridpoint would then be contingent upon the formation of these aggregates, a process which again must be parameterised, occurs on some characteristic timescale, and is in this case represented by ${\zeta^t}_{dec}$. We argue that both of these are plausible mechanisms by which the 'effective dust cover' of a gridpoint may increase over time without the input of any extra dust through deposition. Interestingly, with regard to the second mechanism, Merrison et al. (2007) claimed that the formation of aggregates would require the presence of a certain minimum dust depth, which provides some empirical support for the existence of an inverse relationship between surface dust density and lifting threshold, as has been assumed in this work.

6 Conclusions

Interannual variability in dust storm magnitude and timing of initiation in the UKMGCM was greatly increased by the addition of temporally varying dust lifting thresholds, and a range of peak dust loadings during southern spring and summer were produced during a single multi-year simulation. The increase in variability was attributed to the fluctuation of surface thresholds at several important sites in the southern hemisphere, in response to emission and deposition of dust mass. In fact, the initiation of a major dust storm at one of these sites in a given year was primarily determined by its surface dust sup-

ply, implied through local threshold magnitudes. The continual redistribution of surface dust therefore appears to be a plausible mechanism for forcing atmospheric variability on a multiannual (and possibly multidecadal) timescale. However, internal atmospheric variability ('weather noise') undoubtedly also affects dust lifting, and it is not known how important this is, relative to the surface dust density field, in generating global dust storms. The balance between the two may well have been shifted too heavily in favour of the latter by the parameter values (${\zeta^t}_{inc}$ in particular) chosen in this particular work; however, effectively simulating the effect of surface wind variability is likely to require a more sophisticated treatment of sub-gridscale gustiness than has been attempted to date. The results also illustrate the high sensitivity of modelled dust lifting to the precise choice of threshold, and, therefore, the importance of estimating thresholds accurately.

During a multiannual model simulation, surface dust densities decreased along the latitude band at 30°S and along the northern hemisphere flushing storm channels, locations that have been observed to be covered relatively sparsely by dust at present. Conversely, deposition occurred in the low thermal inertia regions of the NH. This suggests that the current distribution of Martian surface dust can be explained fairly well by the lifting and deposition patterns of the planet's present orbital regime, rather than requiring the invocation of altered transport patterns that may have occurred in previous climates.

At the standard model resolution, net cross-equatorial dust transport was strongly northward, meaning that an artificial resupply term was required in order to prevent the cessation of GDSs after several model years. There was evidence that large dust storms developed too frequently in the southern hemisphere in the model, leading to a loss of dust to the northern hemisphere, and

that southward dust flux during $L_s = 0$–$180°$ may have been underestimated due to inaccuracies in vertical mass profiles in the northern tropics. Changes to cross-equatorial transport rates seen at a higher model horizontal resolution mean that a balance between flushing storm and GDS dust mass flux on the observed timescale of ~ 3 Martian years appears plausible.

Acknowledgements

The authors thank the reviewers, Claire Newman and Jim Murphy, for their detailed comments, from which this manuscript has benefited greatly. DPM thanks John Wilson for suggesting this direction of investigation through his 2009 (published 2010) workshop presentation. This work was funded by the UK Science and Technology Facilities Council.

References

R. A. Bagnold. *The Physics of Blown Sand and Desert Dunes*. Methuen, 1954.

S. Basu, J. Wilson, M. Richardson, and A. Ingersoll. Simulation of spontaneous and variable global dust storms with the GFDL Mars GCM. *J. Geophys. Res. (Planets)*, 111(E10):9004–+, sep 2006. doi: 10.1029/2005JE002660.

F. Forget, F. Hourdin, R. Fournier, C. Hourdin, O. Talagrand, M. Collins, S. R. Lewis, P. L. Read, and J.-P. Huot. Improved general circulation models of the Martian atmosphere from the surface to above 80 km. *J. Geophys. Res.*, 104:24155–24176, oct 1999. doi: 10.1029/1999JE001025.

R. M. Haberle, M. A. Kahre, J. R. Murphy, P. R. Christensen, and R. Gree-

ley. Role of dust devils and orbital precession in closing the Martian dust cycle. *Geophys. Res. Lett.*, 33:L19S04, September 2006. doi: 10.1029/2006GL026188.

N. G. Heavens, M. I. Richardson, A. Kleinböhl, D. M. Kass, D. J. McCleese, W. Abdou, J. L. Benson, J. T. Schofield, J. H. Shirley, and P. M. Wolkenberg. Vertical distribution of dust in the Martian atmosphere during northern spring and summer: High-altitude tropical dust maximum at northern summer solstice. *J. Geophys. Res. (Planets)*, 116:E01007, January 2011. doi: 10.1029/2010JE003692.

J. L. Hollingsworth, R. M. Haberle, J. R. Barnes, A. F. C. Bridger, J. B. Pollack, H. Lee, and J. Schaeffer. Orographic control of storm zones on Mars. *Nature*, 380:413–416, apr 1996. doi: 10.1038/380413a0.

B. J. Hoskins and A. J. Simmons. A multi-layer spectral model and the semi-implicit method. *Quart. J. R. Meteor. Soc.*, 101:637–655, 1975.

M. A. Kahre, J. R. Murphy, R. M. Haberle, F. Montmessin, and J. Schaeffer. Simulating the Martian dust cycle with a finite surface dust reservoir. *Geophys. Res. Lett.*, 32:20204–+, oct 2005. doi: 10.1029/2005GL023495.

M. A. Kahre, J. R. Murphy, and R. M. Haberle. Modeling the Martian dust cycle and surface dust reservoirs with the NASA Ames general circulation model. *J. Geophys. Res. (Planets)*, 111:E06008, June 2006. doi: 10.1029/2005JE002588.

M. A. Kahre, J. L. Hollingsworth, R. M. Haberle, and J. R. Murphy. Investigations of the variability of dust particle sizes in the martian atmosphere using the NASA Ames General Circulation Model. *Icarus*, 195:576–597, jun 2008. doi: 10.1016/j.icarus.2008.01.023.

J. F. Kok. Analytical calculation of the minimum wind speed required to sustain wind-blown sand on Earth and Mars. *ArXiv e-prints*, jan 2010.

J. F. Kok and N. O. Renno. Electrostatics in Wind-Blown Sand. *Phys. Rev. Lett.*, 100(1):014501–+, jan 2008. doi: 10.1103/PhysRevLett.100.014501.

S. R. Lewis, P. L. Read, B. J. Conrath, J. C. Pearl, and M. D. Smith. Assimilation of thermal emission spectrometer atmospheric data during the Mars Global Surveyor aerobraking period. *Icarus*, 192:327–347, dec 2007. doi: 10.1016/j.icarus.2007.08.009.

J. Liu, M. I. Richardson, and R. J. Wilson. An assessment of the global, seasonal, and interannual spacecraft record of Martian climate in the thermal infrared. *J. Geophys. Res. (Planets)*, 108:5089–+, aug 2003. doi: 10.1029/2002JE001921.

O. Martínez-Alvarado, L. Montabone, S. R. Lewis, I. M. Moroz, and P. L. Read. Transient teleconnection event at the onset of a planet-encircling dust storm on Mars. *Annales Geophysicae*, 27:3663–3676, September 2009. doi: 10.5194/angeo-27-3663-2009.

J. P. Merrison, H. P. Gunnlaugsson, P. Nørnberg, A. E. Jensen, and K. R. Rasmussen. Determination of the wind induced detachment threshold for granular material on Mars using wind tunnel simulations. *Icarus*, 191:568–580, November 2007. doi: 10.1016/j.icarus.2007.04.035.

L. Montabone, S. R. Lewis, and P. L. Read. Interannual variability of Martian dust storms in assimilation of several years of Mars global surveyor observations. *Adv. Sp. Res.*, 36:2146–2155, 2005. doi: 10.1016/j.asr.2005.07.047.

C. E. Newman, S. R. Lewis, P. L. Read, and F. Forget. Modeling the Martian dust cycle, 1. Representations of dust transport processes. *J. Geophys. Res. (Planets)*, 107:5123–+, dec 2002a. doi: 10.1029/2002JE001910.

C. E. Newman, S. R. Lewis, P. L. Read, and F. Forget. Modeling the Martian dust cycle 2. Multiannual radiatively active dust transport simulations. *J. Geophys. Res. (Planets)*, 107:5124–+, dec 2002b. doi:

10.1029/2002JE001920.

C. E. Newman, S. R. Lewis, and P. L. Read. The atmospheric circulation and dust activity in different orbital epochs on Mars. *Icarus*, 174:135–160, mar 2005. doi: 10.1016/j.icarus.2004.10.023.

A. A. Pankine and A. P. Ingersoll. Interannual variability of Mars global dust storms: an example of self-organized criticality? *Icarus*, 170:514–518, aug 2004. doi: 10.1016/j.icarus.2004.04.006.

T. E. R. Phillips. Mars, Observations of, in 1924. *Mon. Not. R. Astron. Soc.*, 85:179–+, December 1924.

N. O. Rennó, M. L. Burkett, and M. P. Larkin. A Simple Thermodynamical Theory for Dust Devils. *J. Atmos. Sci.*, 55:3244–3252, November 1998. doi: 10.1175/1520-0469(1998)055¡3244:ASTTFD¿2.0.CO;2.

S. W. Ruff and P. R. Christensen. Bright and dark regions on Mars: Particle size and mineralogical characteristics based on Thermal Emission Spectrometer data. *J. Geophys. Res. (Planets)*, 107:5127–+, dec 2002. doi: 10.1029/2001JE001580.

Y. Shao and H. Lu. A simple expression for wind erosion threshold friction velocity. *J. Geophys. Res.*, 105:22437–22444, sep 2000. doi: 10.1029/2000JD900304.

M. J. Strausberg, H. Wang, M. I. Richardson, S. P. Ewald, and A. D. Toigo. Observations of the initiation and evolution of the 2001 Mars global dust storm. *J. Geophys. Res. (Planets)*, 110(E9):2006–+, feb 2005. doi: 10.1029/2004JE002361.

R. Sullivan, R. Arvidson, J. F. Bell, R. Gellert, M. Golombek, R. Greeley, K. Herkenhoff, J. Johnson, S. Thompson, P. Whelley, and J. Wray. Wind-driven particle mobility on Mars: Insights from Mars Exploration Rover observations at "El Dorado" and surroundings at Gusev Crater. *J. Geophys.*

Res. (Planets), 113:E06S07, June 2008. doi: 10.1029/2008JE003101.

M. A. Szwast, M. I. Richardson, and A. R. Vasavada. Surface dust redistribution on Mars as observed by the Mars Global Surveyor and Viking orbiters. *J. Geophys. Res. (Planets)*, 111(E10):11008–+, nov 2006. doi: 10.1029/2005JE002485.

P. Thomas and P. J. Gierasch. Dust devils on Mars. *Science*, 230:175–177, October 1985. doi: 10.1126/science.230.4722.175.

H. Wang, R. W. Zurek, and M. I. Richardson. Relationship between frontal dust storms and transient eddy activity in the northern hemisphere of Mars as observed by Mars Global Surveyor. *J. Geophys. Res. (Planets)*, 110(E9): 7005–+, jul 2005. doi: 10.1029/2005JE002423.

B. R. White. Soil transport by winds on Mars. *J. Geophys. Res.*, 84:4643–4651, aug 1979. doi: 10.1029/JB084iB09p04643.

R. J. Wilson and M. A. Kahre. The role of spatially variable surface dust in GCM simulations of the Martian dust cycle. In *Mars Dust Cycle Workshop*, pages 108–112, 2010.

M. J. Wolff and R. T. Clancy. Constraints on the size of Martian aerosols from Thermal Emission Spectrometer observations. *J. Geophys. Res. (Planets)*, 108:5097–+, sep 2003. doi: 10.1029/2003JE002057.

M. J. Wolff, M. D. Smith, R. T. Clancy, N. Spanovich, B. A. Whitney, M. T. Lemmon, J. L. Bandfield, D. Banfield, A. Ghosh, G. Landis, P. R. Christensen, J. F. Bell, and S. W. Squyres. Constraints on dust aerosols from the Mars Exploration Rovers using MGS overflights and Mini-TES. *J. Geophys. Res. (Planets)*, 111(E10):12–+, dec 2006. doi: 10.1029/2006JE002786.

R. W. Zurek and L. J. Martin. Interannual variability of planet-encircling dust storms on Mars. *J. Geophys. Res.*, 98:3247–3259, February 1993. doi: 10.1029/92JE02936.